NANO · MICRO small
www.small-journal.com

Highly Perforated V_2O_5 Cathode with Restricted Lithiation toward Building "Rocking-Chair" Type Cell with Graphite Anode Recovered from Spent Li-Ion Batteries

Madhusoodhanan Lathika Divya, Subramanian Natarajan, Yun-Sung Lee, and Vanchiappan Aravindan**

Current research motivation on fabricating next-generation lithium-ion batteries by averting the growing demand for battery raw materials brings enormous interest on the V_2O_5 cathode again as a result of its abundance, ease synthesis, and tunable Li-intercalation properties. So far, the research activities are mainly focused on V_2O_5 to attain a maximum capacity (>300 mAh g^{-1}) for more than 1 mol. Li-intercalation which results in poor structural stability. Keeping this issue in mind, here, the full-cell assembly by limiting 1 mol is proposed and constructed. Li-insertion in V_2O_5 as a cathode and LiC_6 as an anode for the first time. Prior to the full-cell assembly, hydrothermally prepared rod-like V_2O_5 reveals the specific capacity of 143 mAh g^{-1} in half-cell configuration with good cycling stability. The full-cell, V_2O_5/LiC_6, offers a specific capacity of ≈236 mAh g^{-1} with a maximum energy density of ≈197.1 Wh kg^{-1}. Furthermore, the practical feasibility of the cell has been examined at different temperatures that divulged a maximum energy density of 136 Wh kg^{-1} at 50 °C. Also, the obtained results encourage V_2O_5 as a strong contender for the commercial $LiFePO_4$/C system and pave the new directions for advanced battery technology.

1. Introduction

Lithium-ion batteries (LIBs) are still preferable choices among the energy storage devices and bring great interest rapidly to employ in electric vehicles (EV's) and hybrid electric vehicles owing to their high electrochemical performance.[1] On the other hand, the rising demands of emerging technologies badly require next-generation LIBs with high energy density, excellent rate performance, better safety at a lower cost. However, the commercially available $LiCoO_2$ possibly will not remain in place as a preferable cathode material shortly owing to the number of downsides such as toxicity, increasing-price, and growing demand. Also, the limited Li reversible extraction allows $Li_{1-x}CoO_2$ ($x = 0.5$) to deliver a low specific capacity of ≈140 mAh g^{-1}, which daunts their practical application, mainly in EV.[2] Other transition metal oxides such as low-cost $LiNiO_2$ have the struggle to place Li^+ and Ni^{3+} in the structure during synthesis and unstable compared to $LiCoO_2$ even it can acquire high energy density. Spinel $Li_xMn_2O_4$ fronting capacity fading issues as a consequence of the Mn dissolution into the electrolyte, and Li-rich metal oxides can offer a high capacity of >250 mAh g^{-1}, however long-term cyclability is a prime issue and is still in the research bed.[3] Above all, the depletion of current demand battery raw materials such as Ni and Co and its expensiveness hasten to explore the possibility of $LiFePO_4$, which is the most dominant cathode in the olivine type $LiMPO_4$ family.[3,4] Having the advantages of low-cost, nontoxicity, and high safety characteristics, $LiFePO_4$ is also believed to be a top contender as a promising cathode for large-size next-generation LIBs with a practical capacity of ≈150 mAh g^{-1} (3.4 V versus Li). Though the poor electronic conductivity and Li-ion diffusivity are the main interferences, further the low temperature and high rate performances hamper their practical application. Moreover, it is important to note that the $LiFePO_4$ belongs to 3D in the structural aspect, whereas it is considered as 1D in Li-ion transport with the conductivity in the order of 10^{-9} S cm^{-1}. Unfortunately, this insulator type cathode, which is well-known for exceptional thermal stability due to the presence of strong covalent P—O bonds in the $(PO_4)^{3-}$ anions, desperately requires a carbon coating to make it as a conductor for the extraction of one mole Li. In this line, we have attempted to explore the possibility of using layered V_2O_5 as a possible insertion host, which delivers the capacity of ≈143 mAh g^{-1} by insertion of one mol. Li per one V_2O_5. In this regard, V_2O_5 is one of the extensively studied cathode materials and fetches widespread attention in recent years owing to their practicable Li-ion intercalation properties, besides the advantages of high output voltage, easy access of abundant sources, high safety, and admirable energy density.[5–8] As well in contrast to $LiFePO_4$, V_2O_5 belongs to the

M. L. Divya, Dr. S. Natarajan, Dr. V. Aravindan
Department of Chemistry
Indian Institute of Science Education and Research (IISER)
Tirupati 517507, India
E-mail: aravindan@iisertirupati.ac.in, aravind_van@yahoo.com
Prof. Y.-S. Lee
Department of Advanced Chemicals and Engineering
Chonnam National University
Gwangju 61186, Republic of Korea
E-mail: leeys@chonnam.ac.kr
The ORCID identification number(s) for the author(s) of this article can be found under https://doi.org/10.1002/smll.202002624.

DOI: 10.1002/smll.202002624

2D category in both structural and ionic transport aspects and possesses the conductivity in the order of 10^{-3} S cm^{-1} at 25 °C.[9] However, both the materials can be tuned in to 2D structures morphologically. Unless fabricating the carbonaceous composite with $LiFePO_4$, the cathode material could not be able to attain the electrochemical performance of V_2O_5. Therefore, in this particular case, V_2O_5 exhibits better performance characteristics than $LiFePO_4$ and signifies the success of 2D ionic transport pathways of V_2O_5 compared to the 1D channels of $LiFePO_4$. Still, problems exist in improving the cycle life and enhancing the capacity by poor electrical conductivity as a result of V_2O_5 degradation during Li^+ diffusion. At the same time, researchers have been attentive on constructing the V_2O_5 electrode structure to shorten the Li^+ diffusion distance to lift the overall performance of the cell via other different tactics such as synthesizing 1D nanorods, wires, and nanotubes.[10] Though, 3D hierarchical V_2O_5 nanostructures are very protective in terms of structural stability and could able to rush the ion and electron transportation through their porous network. Apart from these approaches, hybridizing the carbons with V_2O_5 could upsurge the electrical conductivity and averting the aggregation. However, such graphene functionalization paves a route to perform the charge transfer process if there is no interface control between V_2O_5 nanoparticles and graphene that distracts the performance. Also, the doping of elements like Ni, Mn, Fe, and Sn into V_2O_5 results in higher electronic conductivity, improved structural stability, rebates the charge transfer resistance as well as fasten the kinetics of Faradic reactions.[10] Nevertheless, cation doping questioning the crystallinity of the electrode material even though it introduced the oxygen vacancies, and there are no clear studies regarding the long-term cycling stability with these approaches. Additionally, it should be noted that the V_2O_5 permits the insertion of three Li^+ and acquires different results in view of rate performance and stability. The V_2O_5 can store two Li^+ and acquires a higher capacity of ≈294 mAh g^{-1} with the help of γ-phase formation between 4.0–2.0 V versus Li, however, by compromising the structural stability.[7,10,11] Most of the studies are reported with more than one mole Li intercalation into a V_2O_5 and achieved the capacity beyond 300 mAh g^{-1}. However, more than two mol. Li-intercalation forms the irreversible ω-$Li_xV_2O_5$ phase when the voltage reaches below 2 V versus Li. Very few works only reported on the limited lithiation to realize the very stable performance.[9] Restricting the lithiation of one mole into V_2O_5 ensures the very stable electrochemical performance (≈143 mAh g^{-1}, ≈3.35 V versus Li) with robust structural features. Interestingly, the electrochemical charge–discharge profiles are highly resembling with the olivine type $LiFePO_4$. The flat charge-discharge profiles of $Li_xV_2O_5$ with 2D Li-ion migration pathways eventually leads to achieving the high-power capability for the LIB power packs. Another important issue is fabricating a V_2O_5 full-cell assembly with a suitable anode, which is a key factor in deciding the practical applications.[12] It is well-known that the usage of lithium metal anode faces severe problems in organic electrolytes and the lithium dendrite formation during the cycling performance easily makes the safety issues in LIBs. Undoubtedly, graphite anode could fulfill the requirements; however, it is a real challenge to construct a full-cell assembly with a Li-free cathode effectively. Although few works reported on the limited lithiation into V_2O_5, nevertheless explore the cathode into the practical configuration is very rare, particularly with graphite. For example, Cheah et al.[13,14] first explored the possibility of fabricating rocking-chair type Li-ion cells with limited lithiation, and later, Ren et al.[15] reported the fabrication of full-cell assembly with $Li_4Ti_5O_{12}$ anode and validated fabricated Li-ion cells with restricted lithiation mode. Nevertheless, the net operating potential is highly limited to 1.9 V only. To date, the graphitic anode has not been utilized to demonstrate the fabrication of "rocking-chair" type Li-ion cells with V_2O_5 cathode with limited lithiation.[9] Theoretically, if we pair the graphite with V_2O_5, it leads to the working potential of 3.3 V, which is quite remarkable, and it is most recommendable as compared to the commercially available $LiFePO_4$/C configuration. Another interesting point to mention here is that no popular transition metals like Ni, Mn, Co, and Fe are employed in this configuration. Further, both graphite and V_2O_5 undergoes the 2D Li-ion pathways, paves a promising feature to explore and high-power Li-ion configuration.[9]

In this work, we have prepared the nanostructured V_2O_5 by a simple hydrothermal treatment; considering the future demand and the increasing price of graphite for various applications, graphite (RG) has been recovered from spent LIBs and reused to evaluate the suitability as an anode in the electrochemically pre-lithiated state (LiC_6). This is the first study; the full cell has been constructed with one mol. Li intercalation using the LiC_6 as an anode with the nanostructured V_2O_5 as a cathode that presents admirable capacity and long-term cycling life, paving a way to build a low-cost and high-performance LIBs for the potential applications in future.

2. Results and Discussion

Nanostructured mesoporous V_2O_5 material was synthesized via a two-step reaction using hydrothermal followed by high-temperature air annealing. The synthesis of nanostructured V_2O_5 in the hydrothermal method is considered as the easiest and most effective way, among other methods. Ammonium metavanadate (NH_4VO_3) was used as the precursor in which vanadium is in the +5 oxidation state yields V_2O_5 on the thermal decomposition after dissolving in H_2SO_4. The solubility of NH_4VO_3 in water is very low, hence the addition of H_2SO_4 increased the solubility and also played a key role as a reductant of vanadium. The dissolution of NH_4VO_3 in acidic solution produces VO_2^+ according to the following equation,

$$VO_3^- (aq) + 4H^+ (aq) + e^- \rightarrow VO^{2+} + 2H_2O \quad (1)$$

The low-temperature hydrothermal process provided a constant reaction atmosphere that resulted in the formation of V_2O_5 red-brown precipitate in the hydrated form (Equation 2). Further heating of the washed sample at 500 °C for 3 h brings about the formation of the yellow-colored shcherbinaite phase of V_2O_5 (Equation 3).

$$2NH_4VO_3 + H_2SO_4 \rightarrow V_2O_5 \cdot xH_2O + (NH_4)_2SO_4 + (1-x)H_2O \quad (2)$$

$$V_2O_5 \cdot xH_2O \rightarrow V_2O_5 \quad (3)$$

The crystallinity and phase purity of the synthesized V_2O_5 sample was analyzed by X-ray powder diffraction using monochromatic CuKα radiation (λ = 1.5406 Å) within the 2θ range of

10–90° at a step of 0.02° as shown in **Figure 1**a. All the peaks in the diffraction pattern match well with an orthorhombic shcherbinaite phase (space group Pmmn No. 59) of V_2O_5 (ICDD 04-008-4555) without any impurity traces, representing the purity of the sample. The sharp and high-intensity peak at $2\theta = 20.12°$ corresponding to the (001) Bragg reflection with an interplanar spacing of 4.413 Å confirms the highly crystalline nature of the sample. The lattice parameter values are calculated to be $a = 11.506$, $b = 3.59$, and $c = 4.413$ Å with the unit cell volume of 182.29 Å^3 which exhibits very close proximity with the standard values of $a = 11.516$, $b = 3.566$, and $c = 4.373$ Å.[16] Using Debye–Scherer's equation, the average crystallite size of the sample (based on the high-intensity peak) was calculated as ≈28 nm. Generally, the V_2O_5 can exist as polymorphic phases such as α-V_2O_5, β-V_2O_5, γ-V_2O_5, and δ-V_2O_5.[17] The Raman spectrum of the synthesized V_2O_5 sample is provided in Figure 1b. The main bands are positioned at 100, 142, 195, 283, 302, 407, 480, 529, 697, and 995 cm^{-1}, and the spectrum is typical for α-V_2O_5.[18,19] The layered arrangement of crystalline V_2O_5 provides the space for the reversible intercalation of Li-ions.

X-ray photoelectron spectroscopy (XPS) technique was used to ascertain the elemental composition and their chemical states at the surface. The survey spectrum shows the peaks for vanadium, oxygen, and carbon (Figure S1, Supporting Information). The low-intensity carbon (C 1s) peak with peak maxima at ≈285 eV is due to adventitious carbon contamination, which is commonly used as charge reference for XPS spectra. The existence of peaks for vanadium (V 2p) at ≈517 and ≈525 eV is attributed to the spin-orbit splitting of the component between V $2p_{3/2}$ (at 517 eV), and V $2p_{1/2}$ (at 525 eV) confirm the composition of V_2O_5,[20] Figure 1c. The O 1s spectrum of the sample, Figure 1d, is deconvoluted into four peaks with binding

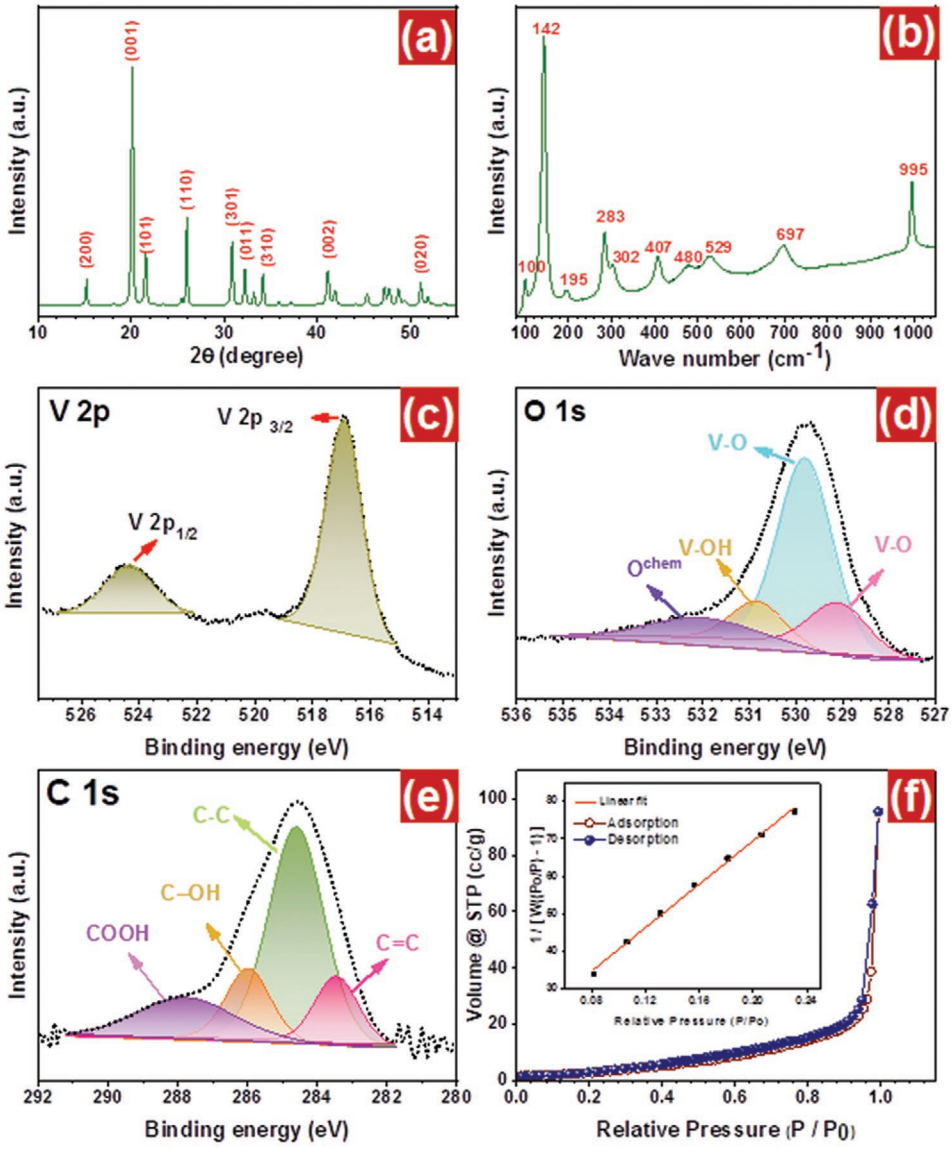

Figure 1. Characterization of V_2O_5 nanostructures: a) XRD pattern, b) Raman spectra, c–e) XPS spectra of V 2p, O 1s, and C 1s, and f) Adsorption Desorption curve by BET analysis.

energies (BE) of ≈529, ≈530, ≈531, and ≈532 eV. The two lower BE peaks at ≈529 and ≈530 eV related to the V—O bonds, (O^{2-} and O^{1-}). The peak positioned at ≈531 eV corresponds to the V—OH bonds. The higher energy peak is assigned to chemically adsorbed oxygen due to surface contamination, mostly from carbon bonds. However, the exact assignments are difficult for high BE peaks in O 1s spectra as they are associated with weakly adsorbed species.[21,22] The C 1s spectrum for adventitious carbon contamination, Figure 1e, contains C—C, C=C, C—OH, and C=O moieties. The BET surface area S_{BET} of the sample was examined by nitrogen adsorption–desorption measurements and is estimated as 11.61 $m^2\ g^{-1}$. The N_2 adsorption-desorption curve of the sample, Figure 1e exhibits Type-IV hysteresis loop with H_3 shape indicates plate-like mesoporous material with slit-shaped connected pores. The pore size distribution was obtained by quenched solid density functional theory and is given in Figure S2, Supporting Information. It could be clearly seen that nanoparticles had a broad mesopore size distribution of 2.5–35 nm, and most of the pores were in the range of 2.5–7 nm. The total pore volume of the sample was calculated as 0.147 $cm^3\ g^{-1}$. The porous nature of the V_2O_5 particles could be attributed to shorten the lithium-ion diffusion pathways and improve the electrochemical kinetics.

The morphology of synthesized V_2O_5 material was studied under different magnification by field emission scanning electron microscopy (FE-SEM) analysis, **Figure 2**a–c. The particles have rod-like morphology with a small fraction of void space between them. The particles have nearly uniform size, and the width and length of the particles are in the range of 100–200 and 200–300 nm, respectively. The detailed structure of a single nanoparticle was analyzed by transmission electron microscopy (TEM) and selected area diffraction (SAED). Figure 2d–e presents the TEM image of a single-particle of length ≈237 nm and width ≈177 nm. The bright diffraction

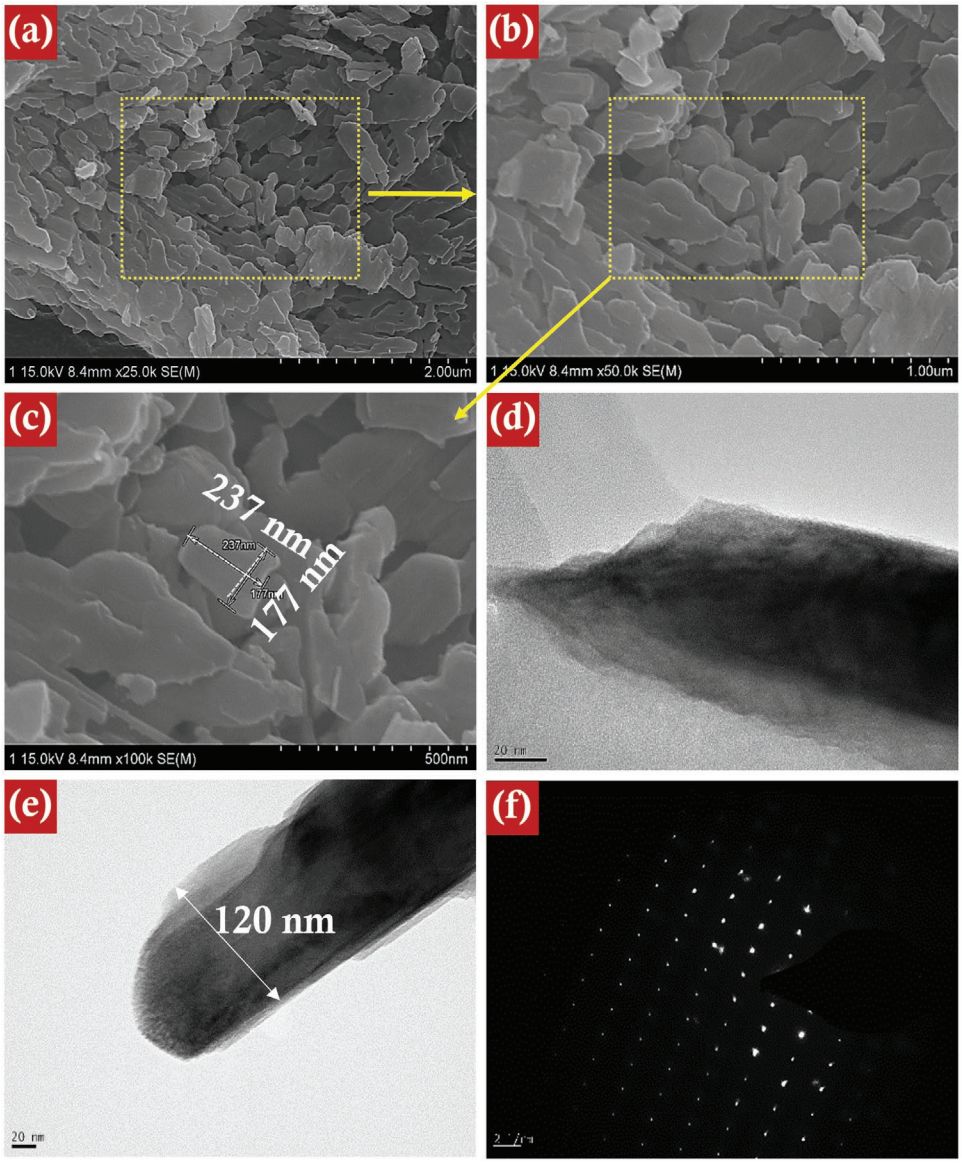

Figure 2. a–c) FE-SEM pictures of V_2O_5 nanostructures with different magnifications, d,e) TEM image, and f) SAED pattern.

spots in the selected area electron diffraction (SAED) pattern, Figure 2f, ensures the single-crystalline nature of V_2O_5 material. The high-resolution transmission electron microscopy (HR-TEM), **Figure 3**a–c, unveils the microporous nature of the material. It shows bright lattice fringes with a lattice spacing of 0.43 nm indicates (001) plane of orthorhombic V_2O_5 phase and confirmed the highly crystalline, layered structure of V_2O_5. The energy dispersive X-ray (EDX) analysis was also performed on the material to ensure purity. TEM-EDX mapping (Figure 3d–g and Figure S3, Supporting Information) further confirmed the presence of elemental carbon along with vanadium and oxygen. No other impurities were observed in the material representing the high purity of material with a small level of ubiquitous carbon at the surface formed during air- annealing of the material. To check the thermal stability of V_2O_5 sample thermal gravimetric analysis (TGA) was performed and result, Figure S4, Supporting Information shows there is only a small weight loss (<1%) below 700 °C, which includes the weight of carbon impurity present in the sample. The presence of carbon is beneficial to improvement in the electrical conductivity of the electrode. As mentioned, the carbon present in the V_2O_5 is very meager; hence, no severe fluctuation is observed upon the TGA measurement.

The half-cells (2016-type coin cells) with metallic Li as the counter electrode in the presence of 1 M $LiPF_6$ in ethylene carbonate (EC): dimethyl carbonate (DMC) as electrolyte were assembled to examine the electrochemical properties of synthesized V_2O_5 material as cathode and RG as an anode. Both galvanostatic and potentiostatic methods were used to investigate the Li-insertion property of the electrode materials. Apparently, the V_2O_5 is a promising cathode for LIB, which involves the typical intercalation due to its layered structure. Upon

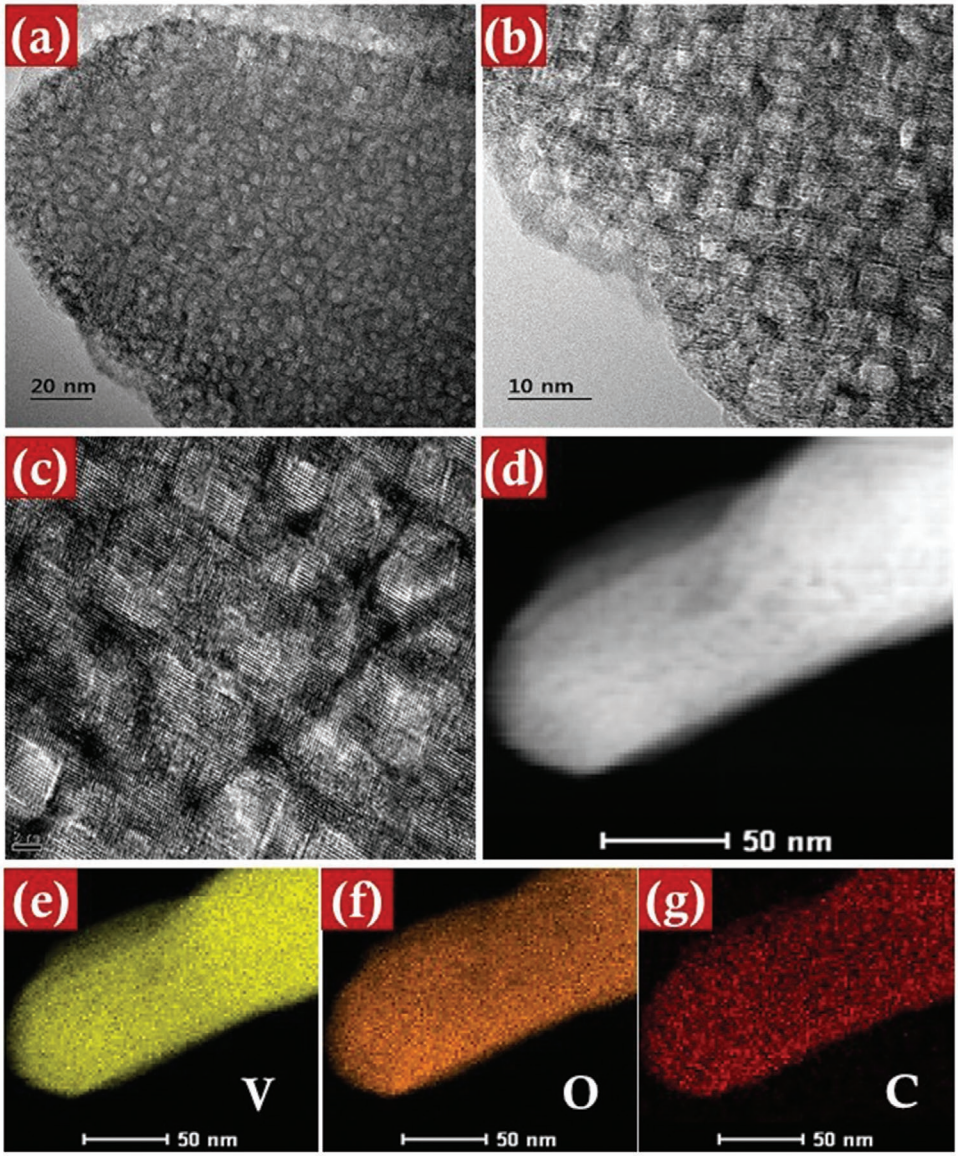

Figure 3. a–c) HR-TEM pictures of V_2O_5 nanostructures with different magnifications, and d–g) TEM-EDS mapping of individual elements.

Li-intercalation into orthorhombic V_2O_5, there is a prominent phase transformation of V_2O_5 into $Li_xV_2O_5$ through the stages of formation of α, ε, δ, γ, and ω phases as a result of multiple electron transfer reactions. The phase of $Li_xV_2O_5$ depends on the number of moles of Li introduced into V_2O_5 lattice such that α phase ($x < 0.1$), ε phase ($0.35 < x < 0.7$) and δ phase ($x = 1$). However, a value of $x > 1$ results in the formation of γ phase ($1 < x < 2$) and irreversible ω phase ($x > 2$) formation. The inserted Li-ions generally reside in the interplanar space between layers of V_2O_5 crystal structure molded by VO_5 octahedral units. It is well known that the V_2O_5 based cell is discharged to a potential <2 V versus Li, that is, lithiation beyond two moles results in a serious distortion in the crystal structure. The robust crystal structure is one of the prerequisites to be employed as an electrode irrespective of anode or cathode. Although it is possible to avoid structural destruction by limiting 2 mol. of Li. However, huge polarization ($\Delta V \geq 1.2$ V) between ≈3.4 V (α to δ) versus ≈2.2 V (γ to ω) region hinders the potential use as an electrode. Therefore, limiting and separating one mol. lithiation leads to the possibility of using V_2O_5 as anode as well as the cathode, that is, ≈3.4 V versus Li as a cathode and ≈2.2 V versus Li as an anode. However, efficient utilization of V_2O_5 as cathode and anode within the 2 mol. Li intercalation process leads to the fabrication of only ≈1.2 V class cells category.[23] This low voltage configuration has no scope for practical applications. Therefore, we attempted to exploit the high voltage region of ≈3.4 V versus Li. On the other hand, promising negative electrode is also required with lithiated state and low redox potential. Options like Sn and Si-based alloy type negative electrodes are certainly possible. However, those anodes still suffer inherent issues like capacity fading, large volume variation, bad surface film formation, etc. Hence, we stick with the well-established graphite, and of course, a promising candidate to employ as an anode. Also, the proposed configuration (V_2O_5/LiC_6) is highly comparable to the $LiFePO_4/C$ configuration in terms of practical capacity and working potential. In fact, the 2D Li-ion migration pathways of V_2O_5 are beneficial over 1D pathways of $LiFePO_4$. The restriction of one mol. lithiation can be realized easily by limiting the lower cut-off potential of 2.5 V versus Li. Cyclic voltammograms (CV) of Li/V_2O_5 half-cell was recorded within the potential window of 2.5–4 V versus Li at a scan rate of 0.1 mV s^{-1} (Figure S5, Supporting Information). Initially, the cell was charged to 4 V versus Li from OCV (above 3 V) to ensure complete oxidation, and subsequently discharged to 2.5 V versus Li for restricted lithiation of one mol. The oxidation/reduction peaks in the cathodic and anodic scan correspond to reversible Li intercalation and deintercalation into the V_2O_5 crystal lattice. The prominent reduction peak located at ≈3.36 V versus Li corresponds to the formation of ε-$Li_{0.5}V_2O_5$ and peak associated with ≈3.16 V versus Li along with a less intense peak at ≈3.1 V versus Li represents the formation of δ-LiV_2O_5 phase. Hence, during the discharge of the cell to 2.5 V versus Li, it results in the reduction of V^{5+} to V^{4+} and the formation of mixed phases like ε-$Li_{0.5}V_2O_5$ and δ-LiV_2O_5. This Li-intercalation process can be explained with the following equations,

$$V_2O_5 + 0.5Li^+ + 0.5e^- \leftrightarrow \varepsilon - Li_{0.5}V_2O_5 \quad (4)$$

$$\varepsilon - Li_{0.5}V_2O_5 + 0.5Li^+ + 0.5e^- \leftrightarrow \delta - LiV_2O_5 \quad (5)$$

The overall equation for restricted lithiation (1 mole) up to 2.5 V versus Li can be written as

$$V_2O_5 + Li^+ + e^- \leftrightarrow LiV_2O_5 \quad (6)$$

Figure S5a, Supporting Information shows the CV traces of Li/V_2O_5 half-cell for the first five cycles. All cycles with prominent and overlapping peaks indicate the high reversibility and cyclability of the Li-ion intercalation/deintercalation in V_2O_5 material. **Figure 4**a depicts the CV traces of Li/V_2O_5 half-cell at various scan rates within the potential window of 2.5–4 V versus Li. As expected, an increase in scan rate increased peak current and peak separation. Further, the CV profile at a low scan rate is clearer due to large contact time, which allows the efficient diffusion of Li-ions to be inserted into the crystal lattice of the material. Figure 4b illustrates a graph that shows a linear relationship between peak current (i_p) and the square root of the scan rate. The chemical diffusion coefficient of Li (D_{Li^+}) in the V_2O_5 material is calculated by the Randles–Sevcik equation and is found to be 5.83×10^{-13} and 8.57×10^{-13} cm^2 s^{-1} corresponding to cathodic and anodic currents, respectively. The Li-ion intercalation and deintercalation in the RG material were also studied by using Li/RG half-cell (OCV: ≈2.8 V versus Li) and given in Figure S5b, Supporting Information. The presence of multiple peaks in the first cathodic scan indicates the intercalation of Li-ions into the graphitic structure in a staging process toward the formation of a graphite intercalation compound, that is, Li_xC_6.[24–26] The peaks present in a voltage higher than 0.5 V versus Li disappeared during the second cycle onward, pointing the formation of a solid electrolyte interface layer on the surface of the graphite electrode. This can also be responsible for high irreversible capacity in the first cycle, mainly due to the decomposition of electrolyte and consumption of Li-ions in an irreversible manner. From the second cycle onward, the cathodic peaks are present only at a potential below 0.2 V versus Li.[27]

The galvanostatic charge–discharge profile of Li/V_2O_5 half-cell was plotted within the potential window of 2.5 to 4 V versus Li at a current density of 100 mA g^{-1} at room temperature. Figure 4c represents the typical charge–discharge profile of V_2O_5 in half-cell configuration, where the cell is exhibiting a discharge capacity of ≈143 mAh g^{-1}, which is approximately equal to the theoretical capacity for restricted lithiation of 1 mol. of Li (≈147 mAh g^{-1}). The position of plateaus in the discharge curve is matching with peak positions of CV traces. The cyclic stability of the cell was tested and depicted in Figure 4d, the cell could deliver a capacity value of ≈97.3 mAh g^{-1} (≈70% of initial capacity) even after 200 charge–discharge cycles. Figure S6a, Supporting Information illustrates the galvanostatic charge–discharge profile of Li/RG half-cell at a current density of 100 mA g^{-1}. The cell showed an initial coloumbic efficiency of 83.12%. However, from the second cycle onward, the cell could exhibit >99% efficiency with a reversible capacity of ≈350 mAh g^{-1}, which is approaching the theoretical discharge capacity of commercial graphite material (≈372 mAh g^{-1}). The cyclic stability of Li/RG half-cell was also tested, Figure S6b, Supporting Information, and it shows a capacity value of ≈294 mAh g^{-1} (83.8% of initial capacity) even after 150 charge–discharge cycles.

In order to analyze the performance of synthesized V_2O_5 with restricted lithiation, the half-cell performance is not at

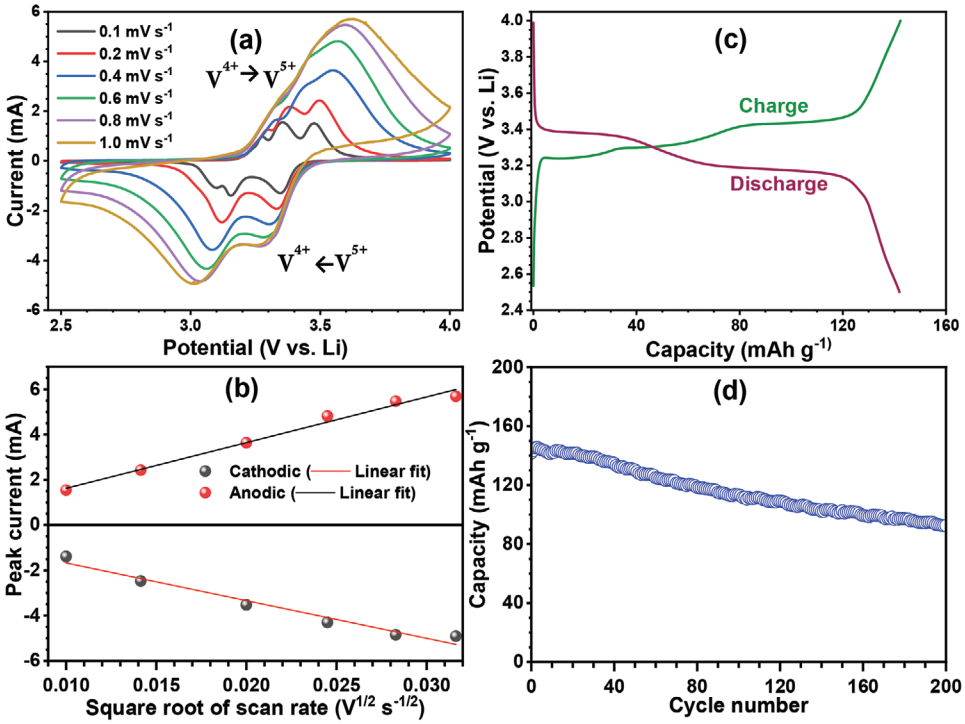

Figure 4. a) CV traces of Li/V_2O_5 half-cell between 2.5 to 4 V at various scan rates, b) Li^+ diffusion calculation, c) typical charge–discharge curves of V_2O_5 in the one mol. restricted lithiation at a current density of 100 mA g^{-1}, and d) plot of reversible capacity versus cycle number at a current density of 100 mA g^{-1}.

all-sufficient. Hence, the full-cell is assembled with RG anode under the balanced mass loading conditions. Prior to the cell assembly, the RG electrode was electrochemically pre-lithiated to form a graphite intercalation compound (LiC_6). The Swagelok assembly was used to construct the half-cell configuration and subjected to three complete discharge–charge cycles, and finally, dismantled in the discharged or lithiated state (LiC_6). The mass loading of V_2O_5 was adjusted to balance the capacity of the RG electrode (mass balance principle). The full-cell assembly (V_2O_5/LiC_6) was done by using a pre-lithiated graphite electrode as anode and V_2O_5 electrode as a cathode by using 1 M $LiPF_6$ in EC: DMC (1:1). The mass ratio of the cathode to anode active material was adjusted to the ratio of ≈2.66: 1 with a total mass of ≈7.52 mg. **Figure 5** depicts the CV profile of V_2O_5/LiC_6 full-cell and is compared with the profiles of both RG and V_2O_5 in half-cell configurations. The appearance of oxidation peaks (at 3.06 and 3.47 V) and reduction peaks (at 3.22 and 3.02 V) represents reversible extraction and insertion of Li -ions within the interplanar space of both lithiated-RG and V_2O_5 electrodes. The peak positions are consistent with that of Li/V_2O_5 half-cell with a small change in potential due to the utilization of the LiC_6 electrode as an anode. The presence of a pair of peaks in V_2O_5/LiC_6 assembly in comparison with three peaks of Li/V_2O_5 half-cell is the influence of the counter electrode, LiC_6, and its polarization. This is quite normal for the case of LiC_6 based systems, and we observed such kinds of behaviors when paired with carbon-coated $LiTi_2(PO_4)_3$[28] and anatase TiO_2 nanofiber cathodes for low-end applications.[29] **Figure 6**a contains the galvanostatic charge–discharge profile for the V_2O_5/LiC_6 cell within the voltage window of 2.4–3.9 V at different current densities (0.1, 0.25, 0.5, 1, 1.5, 2, and 2.5 A g^{-1}). The specific capacity values are calculated based on the mass of anode active material (≈2.08 mg). The cell delivered a maximum specific capacity value of ≈236 mAh g^{-1} at a current density of 0.1 A g^{-1}. Even at a higher current rate of 2.5 A g^{-1}, the cell could exhibit a capacity value of ≈50 mAh g^{-1}. Figure 6b depicts the rate performance of the cell at different current

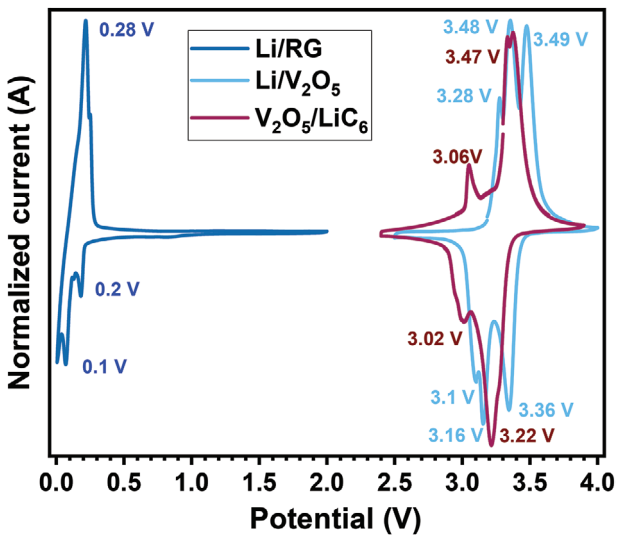

Figure 5. Typical CV traces of V_2O_5/LiC_6 cells between 2.4 to 3.9 V at a scan rate of 0.1 mV s^{-1}. Half-cell performance of RG and perforated V_2O_5 is also given for comparison.

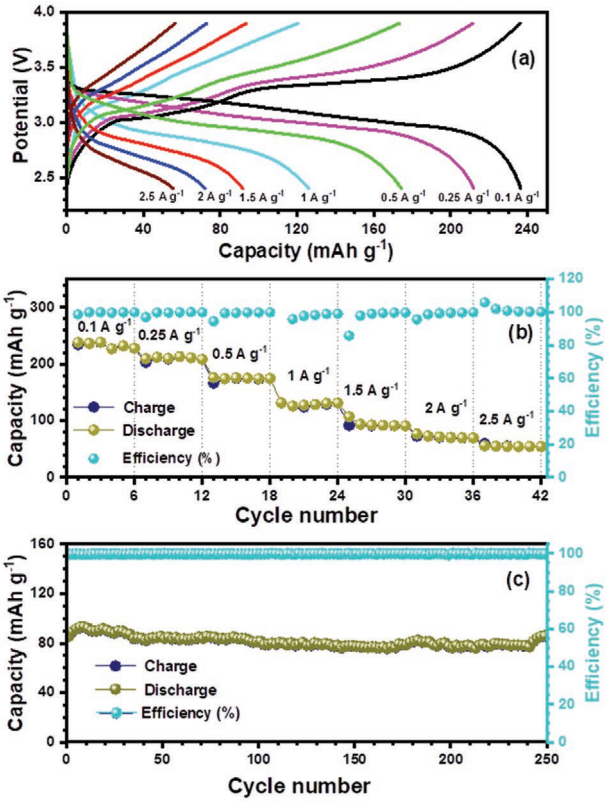

Figure 6. a) Typical galvanostatic charge–discharge curves of V_2O_5/LiC_6 cells between 2.4 to 3.9 V at various current densities, b) Plot of capacity versus cycle number for V_2O_5/LiC_6 cells, in which the capacity is calculated based on the anode mass loading, and c) Plot of capacity versus cycle number at a current density of 1.5 A g^{-1}. The Coloumbic efficiency is also given for the reference.

rates for six cycles each. Lessening the values of capacity at higher current rates is mainly due to low-level ionic penetration at higher rates. Stable performance for several cycles at different current rates indicates high reversible nature of the cell. Long-term cyclic stability of the assembled cell was tested at 1.5 A g^{-1}; Figure 6c illustrates 86.14% of initial capacity retention after 200 charge–discharge cycles with coloumbic efficiency of >99% as a result of the V_2O_5 rod-like morphology with a small fraction of void space between them ensures the low potential drop and better electrochemical performance.

Furthermore, the performance of the assembled V_2O_5/LiC_6 cell was also tested by calculating the energy and power density values by considering the total mass of both anode and cathode active material (7.52 mg). The energy-power density values obtained for different current rates are plotted in the form of a Ragone plot (**Figure 7**). The cell could deliver a maximum energy density value of ≈197.15 Wh kg^{-1} at a power density of 0.316 kW kg^{-1}. At a higher current density of 2.5 A g^{-1}, the cell could deliver a maximum power density of 7.75 kW kg^{-1} with a minimum energy density of 47 Wh kg^{-1}. The performance is superior to the rGO-V_2O_5/lithiated graphite cell,[30] which exhibited an energy density of 106.50 Wh kg^{-1} at a current density of 100 mA g^{-1} for the insertion of more than one mol. Li. In addition to this, to validate the cell performance at different low and high-temperature conditions, the energy storage

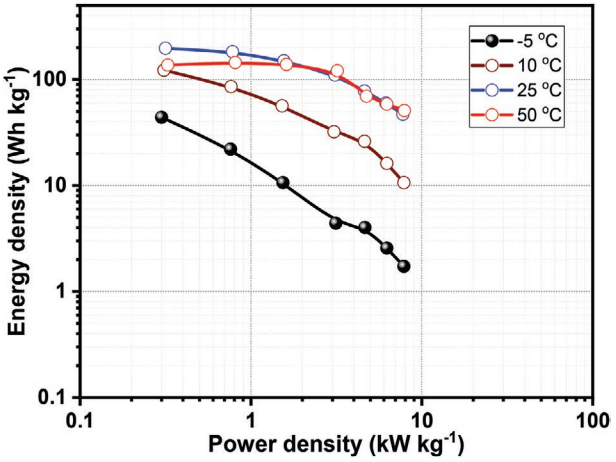

Figure 7. Ragone plot of V_2O_5/LiC_6 cells between 2.4 to 3.9 V at various temperature conditions.

capacity of the cell was tested at various temperature conditions (50, 10, and −5 °C) by placing the cell within the environmental chamber. The cell could deliver a maximum energy density of 136 Wh kg^{-1} @ 0.326 kW kg^{-1}, 122.31 Wh kg^{-1} @ 0.31 kW kg^{-1}, and 43.9 Wh kg^{-1} @ 0.3 kW kg^{-1} at 50, 10, and −5 °C, respectively. Figure S7, Supporting Information illustrates the rate performance of the assembled full-cell at different temperature conditions. The main reason for the declined electrochemical performance of the cell at −5 °C can be explained with reasons like electrolyte crystallization and less mobility of Li^+ ions at sub-zero temperatures. Figure S8a, Supporting Information illustrates the electrochemical impedance spectra (EIS) for both the half-cells, which gives an idea about the interfacial properties of Li-intercalation and deintercalation into synthesized V_2O_5 material and RG material. The charge transfer resistance (R_{ct}) at the electrode–electrolyte interface of Li/V_2O_5 and Li/RG is in the lower range of ≈70 and 30 Ω, respectively. At the same time, the diffusion-limited Warburg impedance is clearly seen in the case of RG. The layered structure with large interplanar space of both the materials, as well as the porous nature of V_2O_5 material, promotes the Li-ion diffusion kinetics and efficient charge transfer. The EIS is recorded for the full-cell assembly (V_2O_5/LiC_6) at different temperature conditions and illustrated in Figure S8b, Supporting Information. The plots further confirm the low and facile Li-ion transport kinetics at sub-zero and high-temperature conditions, respectively. Apparently, a prominent deviation from the solution resistance is also observed with variation in the atmospheric conditions, that is, temperature. Further studies are in progress to understand more in detail and subsequently improve the electrochemical performance of this fascinating configuration.

3. Conclusion

In brief, nanostructured rod-like V_2O_5 was prepared in a facile hydrothermal route and spent LIBs graphite has been reused to employ as an anode material in consideration of the growing demand and environmental contamination. Both V_2O_5 and recovered graphite proclaimed their outstanding

electrochemical performances in the half-cell configuration encouraged to successfully demonstrate the practical feasibility of rocking chair type full-cell assembly for the first time in the restricted lithiation mode. Consequently, the assembled full-cell comprised of nanostructured V_2O_5 and the pre-lithiated graphite (LiC_6) delivered a maximum capacity of ≈236 mAh g^{-1} between 2.4 —3.9 V at a current density of 0.1 A g^{-1}, and the cell assurances the excellent rate performance with excellent cycling stability. Notably, the V_2O_5/LiC_6 cell could able to attain a maximum energy density of ≈197.15 Wh kg^{-1} at a power density of 0.316 kW kg^{-1}, and the temperature performance studies further explored the possibility of using them in practical applications. As a result, this configuration is strongly approaching to substitute the commercially available $LiFePO_4$/C in the market for various applications and paving a route to construct low-cost energy storage devices.

4. Experimental Section

Synthesis of Electrode Materials: The cathode active material, V_2O_5, was synthesized by the facile hydrothermal route, similar to the previously reported study.[31] In a typical process, 0.012 mols of ammonium metavanadate was added to 60 mL of Milli Q water and magnetically stirred with the dropwise addition of concentric H_2SO_4 until the solution color turns to dark orange. Then, the solution was transferred to 100 mL Teflon- lined autoclave and was heated at 200 °C for 24 h. Further, the reactor was removed and cooled naturally; the reaction product was washed with water and centrifuged for 10 min until the pH became neutral. Subsequently, the product was washed with ethanol and dried in a vacuum oven. The final calcination of the resultant powder was carried out at 500 °C for 3 h to ensure the complete oxidation in the box furnace under air atmosphere.

As reported in a previous study,[32–35] graphite from spent LIB anode (Cu foil with graphite paste), was separated by a simple sonication process followed by multistage leaching using water and DMF (in the last stage) as solvents. The recovered graphite (RG) material was washed and oven-dried at 60 °C before using it as the anode active material for the fabrication of full-cell assembly.

Characterization: The crystallinity and phase purity of synthesized V_2O_5 nanostructure were characterized by X-ray diffraction (XRD, ULTIMA IV, Rigaku, ARBL-RAD) and Raman spectroscopy (LabRam HR800 UV Raman microscope, Horiba Jobin- Yvon, France), respectively. The XPS (Multilab 2000, UK) measurements were recorded to visualize the elemental composition and surface functional groups. The surface area of the prepared material was obtained by the BET surface area analyzer, Quantachrome Autosorb and Measured at liquid nitrogen temperature (77 K). Surface morphology and microstructure of the sample were recorded with FE-SEM (S-4700, Hitachi, Japan) and HR-TEM (JEM-2000, EX-II, JEOL, Japan), respectively. Energy-dispersive X-ray spectroscopy (EDS) was used to analyze the elemental composition of the material. The purity and composition of the synthesized material were also tested by TGA.

Cell Fabrication: The full-cell was fabricated with synthesized V_2O_5 nanostructure as a cathode and recovered graphite as anode material. The composite V_2O_5 electrode was made by mixing the V_2O_5, conductive carbon (acetylene black), and binder (teflonized acetylene black TAB-2) in the ratio 70: 20: 10 with mortar and pestle using ethanol. Then, the composite material was pressed on a 14 mm diameter stainless steel mesh current collector (Goodfellow, UK) and was dried for a minimum of 4 h in a vacuum chamber. For the fabrication of the RG electrode, 80% of active material was mixed with 10% conductive carbon (acetylene black) and 10% binder (polyvinylidene fluoride), and was made in the form of a homogeneous slurry with N-methyl pyrrolidone solvent. Further, the slurry was kept under constant magnetic stirring overnight to obtain a homogeneous mixture. The slurry was coated on to Cu foil and was dried overnight and pressed under hot roll press (Tester Sangyo, Japan). Disc electrodes of 14 mm diameter and with an average of ≈2 mg active material was punched out using an electrode cutter. Before the cell assembly, the electrodes were dried at 75 °C for 4 h under vacuum. The cells (both half-cells and full-cell) were fabricated in the form of coin cells (CR 2016) in Ar filled glove box. 1 M $LiPF_6$ in EC:DMC (1:1, v/v) electrolyte (Tomiyama, Japan) and Whatman paper (1825-047, GF/F) separator were used for all the cell assemblies. The half-cells were fabricated with V_2O_5/RG electrodes with the Li metal counter electrode. The full-cell assembly was done with a pretreated V_2O_5 electrode as the cathode and electrochemically pre-lithiated graphite (LiC_6) electrode as an anode.

Electrochemical Measurements: Battery tester, BCS 805 (Biologic France), was used to study the electrochemical performance of the assembled coin cells. CV of both half-cells and the full-cell was recorded at 0.1 mV s^{-1}. The diffusion coefficient of Li-ions in V_2O_5 half -cell assembly was calculated from the CV profile at different scan rates. Galvanostatic charge–discharge studies were performed within the voltage window of 2.5–4 V for Li/V_2O_5 half-cell and 0.005–2.00V for Li/RG half-cell at a current density of 100 mA g^{-1}. For the full-cell assembly, both the electrodes were paired with Li in half-cell assembly using Swagelok fittings for pretreatment. The RG electrode was dismantled in the discharge state, which indicates the formation of electrochemically pre-lithiated RG electrode (LiC_6).[36] The mass of active material loading in the V_2O_5 electrode was adjusted to balance the discharge capacity of both the half-cells. EIS was performed with an applied amplitude of 10 mV in the range of 10 kHz to 1 Hz. The energy and power density values of assembled V_2O_5/LiC_6 cells were calculated at different current rates and was represented in the form of Ragone plot. The electrochemical performance of the cell at different temperature conditions was also done with the help of an environmental chamber (Espec, Japan).

Supporting Information

Supporting Information is available from the Wiley Online Library or from the author.

Acknowledgements

M.L.D and S.N. contributed equally to this work. M.L.D. wishes to thank the funding through Women Scientist Scheme-B (DST/WOS-B/2018/2039) from the KIRAN division of the Department of Science & Technology (DST), Govt. of India. V.A. acknowledges financial support from the Science & Engineering Research Board (SERB), a statutory body of the DST, Govt. of India, through the Ramanujan Fellowship (SB/S2/RJN-088/2016). Y.S.L. acknowledges the financial support from the National Research Foundation of Korea (NRF) grant funded by the Korea government (Ministry of Science, ICT & Future Planning) (No. 2019R1A4A2001527).

Conflict of Interest

The authors declare no conflict of interest.

Keywords

graphite, layered V_2O_5, lithium intercalation, lithium-ion batteries, rocking-chair type

Received: April 26, 2020
Revised: August 13, 2020
Published online: October 13, 2020

[1] N. Nitta, F. Wu, J. T. Lee, G. Yushin, *Mater. Today* **2015**, *18*, 252.
[2] K. Mizushima, P. C. Jones, P. J. Wiseman, J. B. Goodenough, *Mater. Res. Bull.* **1980**, *15*, 783.
[3] V. Aravindan, J. Gnanaraj, Y.-S. Lee, S. Madhavi, *J. Mater. Chem. A* **2013**, *1*, 3518.
[4] A. K. Padhi, *J. Electrochem. Soc.* **1997**, *144*, 1188.
[5] M. S. Whittingham, *Chem. Rev.* **2004**, *104*, 4271.
[6] N. A. Chernova, M. Roppolo, A. C. Dillon, M. S. Whittingham, *J. Mater. Chem.* **2009**, *19*, 2526.
[7] Y. L. Cheah, N. Gupta, S. S. Pramana, V. Aravindan, G. Wee, M. Srinivasan, *J. Power Sources* **2011**, *196*, 6465.
[8] P. Thamodaran, T. Kesavan, M. Vivekanantha, B. Senthilkumar, P. Barpanda, M. Sasidharan, *ACS Appl. Energy Mater.* **2019**, *2*, 852.
[9] S. Natarajan, S.-J. Kim, V. Aravindan, *J. Mater. Chem. A* **2020**, *8*, 9483.
[10] J. Yao, Y. Li, R. C. Massé, E. Uchaker, G. Cao, *Energy Storage Mater.* **2018**, *11*, 205.
[11] M. L. Divya, V. Aravindan, *Chem. - Asian J.* **2019**, *14*, 4665.
[12] V. Aravindan, Y.-S. Lee, S. Madhavi, *Adv. Energy Mater.* **2015**, *5*, 1402225.
[13] Y. L. Cheah, V. Aravindan, S. Madhavi, *J. Electrochem. Soc.* **2013**, *160*, A1016.
[14] Y. L. Cheah, V. Aravindan, S. Madhavi, *ACS Appl. Mater. Interfaces* **2013**, *5*, 3475.
[15] X. Ren, Y. Zhai, L. Zhu, Y. He, A. Li, C. Guo, L. Xu, *ACS Appl. Mater. Interfaces* **2016**, *8*, 17205.
[16] Y. Yue, H. Liang, *Adv. Energy Mater.* **2017**, *7*, 1602545.
[17] T. K. Le, M. Kang, S. W. Kim, *Ceram. Int.* **2019**, *45*, 15781.
[18] F. Urena, A. Crunteanu, J.-P. Raskin, *Appl. Surf. Sci.* **2017**, *403*, 717.
[19] M. B. Smirnov, E. M. Roginskii, K. S. Smirnov, R. Baddour-Hadjean, J.-P. Pereira-Ramos, *Inorg. Chem.* **2018**, *57*, 9190.
[20] M. C. Biesinger, L. W. M. Lau, A. R. Gerson, R. S. C. Smart, *Appl. Surf. Sci.* **2010**, *257*, 887.
[21] J.-C. Dupin, D. Gonbeau, P. Vinatier, A. Levasseur, *Phys. Chem. Chem. Phys.* **2000**, *2*, 1319.
[22] L. Q. Wu, Y. C. Li, S. Q. Li, Z. Z. Li, G. D. Tang, W. H. Qi, L. C. Xue, X. S. Ge, L. L. Ding, *AIP Adv.* **2015**, *5*, 097210.
[23] C. Liu, E. I. Gillette, X. Chen, A. J. Pearse, A. C. Kozen, M. A. Schroeder, K. E. Gregorczyk, S. B. Lee, G. W. Rubloff, *Nat. Nanotechnol.* **2014**, *9*, 1031.
[24] S. Jayaraman, G. Singh, S. Madhavi, V. Aravindan, *Carbon* **2018**, *134*, 9.
[25] S. Jayaraman, S. Madhavi, V. Aravindan, *J. Mater. Chem. A* **2018**, *6*, 3242.
[26] M. Winter, J. O. Besenhard, M. E. Spahr, P. Novák, *Adv. Mater.* **1998**, *10*, 725.
[27] L. Tian, Q. Zhuang, J. Li, Y. Shi, J. Chen, F. Lu, S. Sun, *Chin. Sci. Bull.* **2011**, *56*, 3204.
[28] V. Aravindan, M. Ulaganathan, W. C. Ling, S. Madhavi, *ChemElectroChem* **2015**, *2*, 231.
[29] S. Jayaraman, V. Aravindan, N. Shubha, M. Ulaganathan, S. Madhavi, *Part. Part. Syst. Charact.* **2016**, *33*, 306.
[30] N. Xu, J. Liang, T. Qian, T. Yang, C. Yan, *RSC Adv.* **2016**, *6*, 98581.
[31] B. B, I.-H. Cho, J.-S. Bak, H.-J. Kim, *New J. Chem.* **2018**, *42*, 11862.
[32] S. Natarajan, D. Shanthana Lakshmi, H. C. Bajaj, D. N. Srivastava, *J. Environ. Chem. Eng.* **2015**, *3*, 2538.
[33] K. Subramanyan, S. Natarajan, Y.-S. Lee, V. Aravindan, *Chem. Eng. J.* **2020**, *397*, 125472.
[34] S. Natarajan, V. Aravindan, *Adv. Energy Mater.* **2018**, *8*, 1802303.
[35] M. L. Divya, S. Natarajan, Y.-S. Lee, V. Aravindan, *J. Mater. Chem. A* **2020**, *8*, 4950.
[36] V. Aravindan, Y.-S. Lee, S. Madhavi, *Adv. Energy Mater.* **2017**, *7*, 1602607.